Demonstration of Frequency-Scanning Burst-mode Filtered Rayleigh Scattering for Multi-Parameter Gas-Phase Measurements

Amanda M. Braun[1]
Purdue University, West Lafayette, Indiana 47907 USA

Neil S. Rodrigues[2], Paul M. Danehy[3]
NASA Langley Research Center, Hampton, Virginia 23666 USA

Alexander R. Suppiah[4],
Purdue University, West Lafayette, Indiana 47907 USA

James Braun[5],
North Carolina State University, Rayleigh, North Carolina 27695 USA

Mikhail N. Slipchenko[6], and Terrence R. Meyer[7]
Purdue University, West Lafayette, Indiana 47907 USA

Filtered Rayleigh scattering (FRS) is a diagnostic technique used for measurements of macroscopic properties of a gas. The FRS signal is passed through a narrow bandwidth molecular filter, commonly gaseous iodine, to measure the broadening and Doppler-shift of the scattering light from the molecules of the gas flow. However, in single-frequency, intensity-based approaches, the effects of pressure, temperature, and velocity can be difficult to deconvolve. To overcome this challenge, frequency-scanning FRS has been used to quasi-spectrally resolve the signal. In this work, a frequency-scanned, burst-mode laser was used to perform scanning FRS in an underexpanded jet to measure temperature, pressure, and radial velocity at measurement rates up to 1 kHz which is ~100,000 times faster than prior implementations of scanning FRS.

I. Introduction

Gas-phase measurements of temperature, pressure, and velocity are crucial for computational and empirical model validation for the design of complex space and aeronautical vehicles. Laser-based techniques can provide non-intrusive *in situ* measurements in the relevant flow fields created by ground test facilities. However, one challenge in implementing these techniques is that most ground tests are performed in wind tunnels that contain only air or nitrogen

[1] Graduate Research Assistant, School of Mechanical Engineering, AIAA Member, braun39@purdue.edu.
[2] Optical Physicist, Advanced Measurements and Data Systems Branch, AIAA Member.
[3] Senior Technologist, Advanced Measurements and Data Systems Branch, AIAA Associate Fellow.
[4] Undergraduate Student, School of Mechanical Engineering.
[5] Assistant Professor, School of Mechanical and Aerospace Engineering, AIAA Member.
[6] Research Professor, School of Mechanical Engineering, AIAA Member.
[7] Professor, School of Mechanical Engineering, Associate Fellow.

within the freestream. Techniques such as particle image velocimetry (PIV), Doppler global velocimetry (DGV), or planar laser induced fluorescence (PLIF) often require seeding the flow with particulates or fluorophores to make measurements. Rayleigh scattering (RS), on the other hand, does not require seeding and can be performed directly on the flow molecules with any laser wavelength [1]. In comparison to the incident laser spectral profile, the RS spectrum can be Doppler-broadened, collisional-broadened, or Doppler-shifted due to the temperature, pressure, density, or velocity of the flow, respectively, potentially enabling simultaneous multi-parameter measurements [1].

Filtered Rayleigh scattering (FRS) is a variation of RS that utilizes a spectrally narrow molecular filter (usually iodine for 532 nm excitation) to spectrally-resolve the RS signal or to remove stray light scattering [2]. However, single-wavelength, intensity-based FRS requires additional information to distinguish between the effects of pressure, temperature, and velocity on the signal intensity. This can be accomplished by using multiple camera angles [3, 4] as well as cameras coupled with iodine cells set to different conditions [5]. Another approach is to use multiple incident central laser frequencies, which has been demonstrated for time-averaged, multi-parameter measurements in supersonic flows [2, 6], ducted flows [7], and turbulent jets [8]. In this methodology, only a single camera and iodine cell are required for the determination of pressure, temperature, and single velocity component, which may be less costly, more robust, and more practical in large facility tests.

Previous work with frequency scanning has been limited to data collection times on the order of minutes: Forkey *et al*. reported typical test runs of ~50 minutes, although subsequently decreased that time to as little as 3 minutes [6], and Doll *et al*. reported 12 minutes per test run [7]. More recently, frequency-scanned burst-mode lasers (BML) have allowed for increased measurement rates for DGV [9], as well as NO-PLIF [10], and have been implemented for DGV velocity measurements in a wind tunnel environment [11]. In this paper, the implementation of a burst-mode laser for frequency-scanning FRS is introduced and characterized to enable rapid multi-parameter measurements for short-duration testing. The technique is then demonstrated in an underexpanded jet flowfield for simultaneous measurement of temperature, pressure, and radial velocity with decreased measurement duration by 100,000x, down to 1 to 5 ms per scan. The potential for further improvements in measurement rate is also discussed.

II. Experimental Systems

A. Underexpanded jet system

An underexpanded free-jet apparatus, previously described in [12, 13], was used for measurements of a sonic nozzle featuring a ~2.67±0.01 mm diameter orifice. A mass flow controller (Alicat; MCRS-1000SLPM-D/5M) was used to change the stagnation pressure, which was measured with a pressure transducer (Omega; PX409-250A5V) within the plenum. A thermocouple was also installed in the plenum to measure the plenum temperature. A LabView virtual instrument was used to record the average mass flow rate, plenum temperature, and plenum pressure for each test. Air was provided by the ~830-kPa (120-psi) facility air supply which provided a maximum flow rate of 450 SLPM for the current nozzle diameter. The nozzle pressure ratio (NPR) was defined as:

$$\mathrm{NPR} = P_0/P_A \tag{1}$$

where P_A is the ambient pressure of 101.325 kPa (14.7 psia) for standard atmospheric conditions and P_0 is the measured stagnation pressure in the plenum. The plenum pressure and temperature were monitored to ensure that steady-state operating conditions were established before data collection (usually around 1 to 2 minutes after adjusting the mass flow rate). Schlieren imaging, shown in Fig. 1, depicts the characteristic flow features such as the Mach disc and barrel shock of an underexpanded jet for three different NPR values.

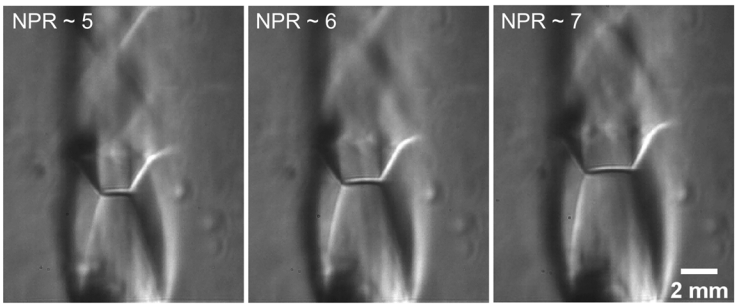

Fig. 1 Schlieren imaging of the underexpanded jet operating at increasing NPRs.

B. Frequency-scanning burst-mode FRS system

The experimental apparatus and laser system used in this work is depicted in Fig. 2. A custom Spectral Energies, LLC Quasimodo Burst-Mode laser (BML), which is based on a well-established master oscillator power amplifier (MOPA) architecture, was utilized. The master oscillator consisted of a continuous wave (cw) diode laser sliced into 10 ns pulses using fiber-coupled acousto-optic modulators (AOMs). Before pulse slicing, a voltage ramp generated by a function generator (Wavetek; Model 23) was applied to the diode laser current to scan the laser seed frequency. The laser frequency was scanned ~6 GHz across a fairly isolated absorption line near 18789.28 cm^{-1}, which was also used in [2]. The frequency-scanned pulse train was then routed into the power amplifier stage consisting of sequential, flashlamp-pumped Nd:YAG rods where the pulses were amplified in "bursts" of a given duration, typically 1 or 5 ms in the current work.

After the second harmonic generation (SHG) in a noncritical phase-matching LBO (LiB_3O_5) crystal, a small portion of the 532 nm beam was routed into the Frequency Monitoring leg (dashed box in Fig. 2) using a polarizing beam splitter (PBS) and half wave plate (HWP) to attenuate the amount of light. In this leg, most of the beam was sent into another PBS and HWP to further attenuate the light and fiber-coupled into a high-speed wavemeter (HighFinesse; HF-WF6-600 VIS) capable of measuring wavelength at a maximum rate of 24 kHz. A wedged window was used to pick off a small portion of the beam before the wavemeter. This reflection was attenuated with a PBS, then split 50/50 with a non-polarizing beam splitter (BS) to be focused onto a reference photodiode (PD) as well as through an iodine cell (ISSI; I2M-5) and onto a second PD.

The rest of the total output beam was routed through a final HWP to maximize the Rayleigh scattering signal. The ~9.5 mm diameter laser beam was focused into a laser sheet with a +300 mm focal length cylindrical lens and passed through the jet flow in the -y-direction (see dotted box). An iris (IR) was used to reduce scatter from the nozzle surface. The resulting Rayleigh scattering was captured with a 50/50 BS cube, with half of the light directed onto a pair of unfiltered high-speed cameras (Photron; Fastcam SA-Z): one unfiltered and one filtered by coupling with an iodine cell (ISSI; I2M-5). The two iodine cells used in this work were held at 70-degrees Celsius with fill conditions of 1 torr at 40-degrees Celsius. Both high-speed cameras had 150 mm focal length lenses (IRIX; DSLR Full Frame Macro 1:1 Lens) with the aperture set to *f*/2.8. The unfiltered camera was used to account for pulse-to-pulse energy variations during the burst, as well as spatial variation in the laser sheet profile, and to provide instantaneous density measurements. Voltage signals from the reference photodiode, filtered photodiode, camera recording, and wavemeter exposure were captured on an oscilloscope to provide a wavelength reference and aid in timing. In this scattering collection configuration, depicted as a vector diagram in Fig. 2, the velocity sensitivity will be along the vector ***k*** (red color). The radial velocity, defined as positive in the +y-direction can be computed from the velocity component in the k-direction based on the Doppler shift.

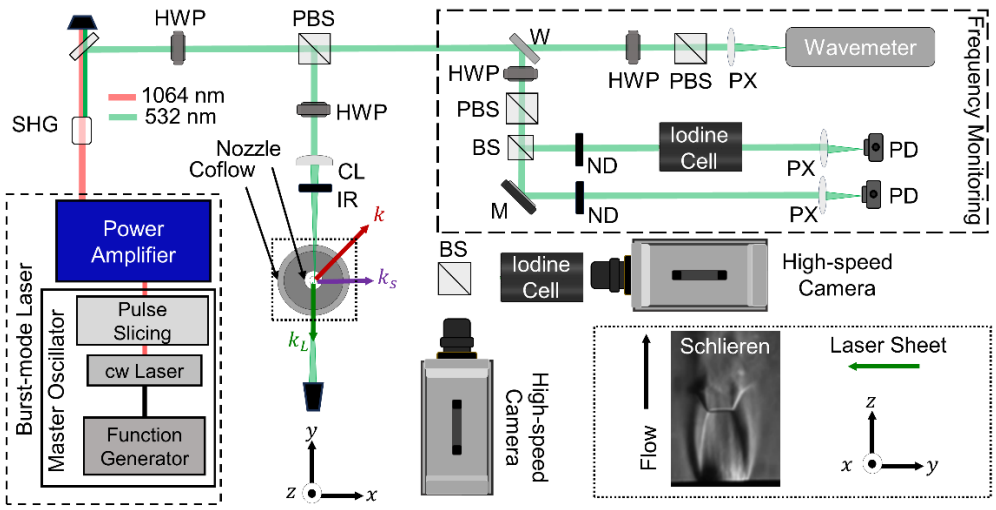

Fig. 2 Experimental setup for unfiltered and filtered Rayleigh scattering in an underexpanded jet. Vector diagram shows the velocity sensitivity direction, k, which is the difference between the scattering vector, k_S, and the incident laser vector, k_L. Orientation of laser sheet and flow direction are depicted in the dotted box. SHG – second harmonic generation crystal; HWP – half wave plate; PBS – polarizing beam splitter; W – wedged window; PX – plano-convex focusing spherical lens; PD – photodiode; CL – cylindrical lens; BS – non-polarizing 50/50 beam splitter.

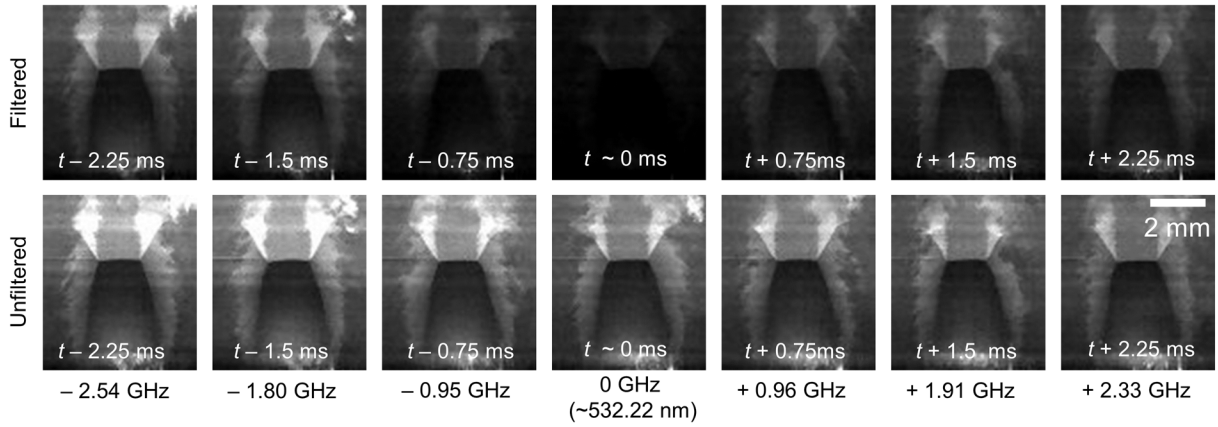

Fig. 3 Filtered and unfiltered Rayleigh scattering images during a laser frequency scan showing every 15th image where t ~ 0 ms is near the center of the absorption line. The corresponding laser pulse wavelength is shown below each image.

Using a laser repetition rate of 20 kHz with a burst duration of 5 ms and a 200 Hz ramp voltage modulation, raw filtered and unfiltered images are shown in Fig. 3 at 0.75 ms spacing to show the signal changing as the laser frequency is tuned across the iodine absorption line while the jet is operating at an NPR of ~7.

Two laser configurations were compared and are described in Table 1. Configuration 1, depicted in Fig. 3, was a single scan of the laser frequency across a 5-ms burst. With the laser repetition rate of 20 kHz, this yielded one flow measurement per burst with ~100 pulses at a per-pulse energy of ~860 mJ. Each pulse within the burst was measured by the high-speed wavemeter. In Configuration 2, the laser repetition rate was increased to 200 kHz while the burst duration was decreased to 1 ms. Using now a 1 kHz ramp modulation, this configuration provided ~200 pulses with ~280 mJ/pulse and one measurement acquired within 1-ms. When the laser repetition rate was increased in Configuration 2, every 10th pulse could be measured with the wavemeter and linear interpolation was used to determine the wavelength of the pulses in between. The output of the Frequency Monitoring leg for each configuration is shown in Fig. 4.

Table 1 Configurations of the frequency-scanning burst-mode laser.

Configuration	Laser (kHz)	Burst (ms)	Modulation (Hz)	Pulses/Scan	Scans/Burst	532 nm Energy/Pulse (mJ)
1	20	5	200	100	1	860
2	200	1	1000	200	1	280

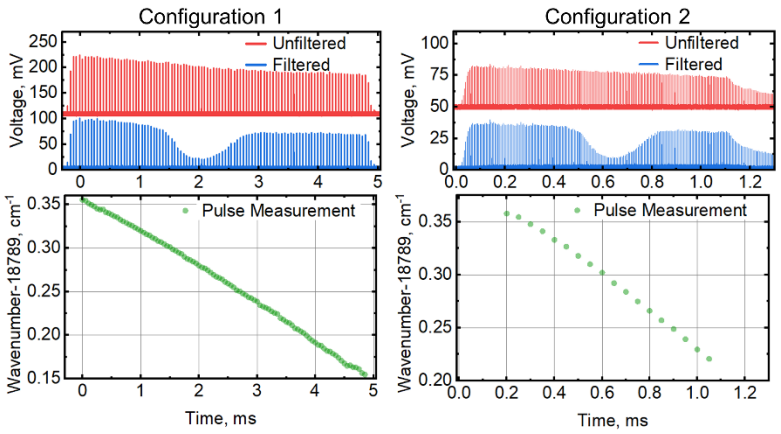

Fig. 4 Unfiltered and filtered burst profiles with corresponding wavemeter pulse measurements for (Left) Configuration 1 and (Right) Configuration 2.

III. Data Processing Methodology

A. Image Processing

The four image processing steps that were performed on both the filtered and unfiltered image are depicted for a single set of frames in Fig. 5. For the entirety of this work, the 12-bit images extracted from the high-speed cameras were converted to 16-bit for processing and, hence, the counts correspond to a 16-bit scale. Initially, each raw image from the filtered and unfiltered cameras was flatfield and darkfield corrected to account for illumination variation. Uniformly illuminated images of a screen were captured to generate flatfield images at the camera resolution used for each camera. Equation (2) was then applied to each image in the burst on each camera, given by:

$$\boldsymbol{C} = \frac{\boldsymbol{R}-\boldsymbol{D}}{\boldsymbol{F}-\boldsymbol{D}}\, m \tag{2}$$

where $\boldsymbol{C}$ is the corrected image matrix, $\boldsymbol{R}$ is the raw image matrix, $\boldsymbol{D}$ is the darkfield image matrix which was generated by taking the mean of a set of 50 images without laser illumination, $\boldsymbol{F}$ is the mean flatfield image matrix, and m is the mean scalar value of $(\boldsymbol{F}-\boldsymbol{D})$.

Next, a dust removal algorithm was implemented to remove bright signals caused by scattering from dust particles that were present in the field of view (FOV). The image was binarized using a threshold value of ~80% of the maximum possible intensity (4096 for a 12-bit camera). Pixels with intensity levels that exceeded the threshold were replaced with a linearly interpolated value of the surrounding pixels. Dust removal was mainly implemented to avoid introducing errors in the laser sheet correction step. The misalignment in FOV between the filtered and unfiltered cameras was accounted for using intensity-based image registration. The filtered images were set as the "target" FOV. Then, the unfiltered images were transformed using affine transformation which allows for translation, rotation, scale, and shear on an image-by-image basis to match the FOV of the filtered images.

Finally, a spatial laser sheet and energy correction was performed on an image-by-image basis to correct for intensity striations present in the laser sheet, the Gaussian spatial profile of the laser sheet, and overall pulse-to-pulse energy variation across the burst. A region of unaffected air Rayleigh signal to the right of the nozzle exit in the unfiltered camera was averaged into a column of values. This was repeated for the entire set of images in the burst, and then each column was normalized by the mean intensity value of the entire burst. Each pixel of both the unfiltered and filtered camera images was then divided on row-by-row basis by this normalized value to eliminate the intensity variations and correct for the overall slope of the burst profile. Correcting both the filtered and unfiltered images by the unfiltered image intensity profile was necessary because the filtered camera signal intensities were a function of both the incident laser energy and the laser frequency with respect to the absorption band.

During data collection, it was noticed that the nozzle exit plane moved in the positive z-direction with increasing plenum pressure. To account for this, an average was taken of the filtered camera images for each PR. Using a small amount of surface scattering from the nozzle surface, the nozzle exit plane was approximated by taking the gradient of the centerline pixel intensities. The row of pixels with the maximum gradient was taken as the nozzle surface location which had a 1-pixel vertical difference between the three NPRs tested.

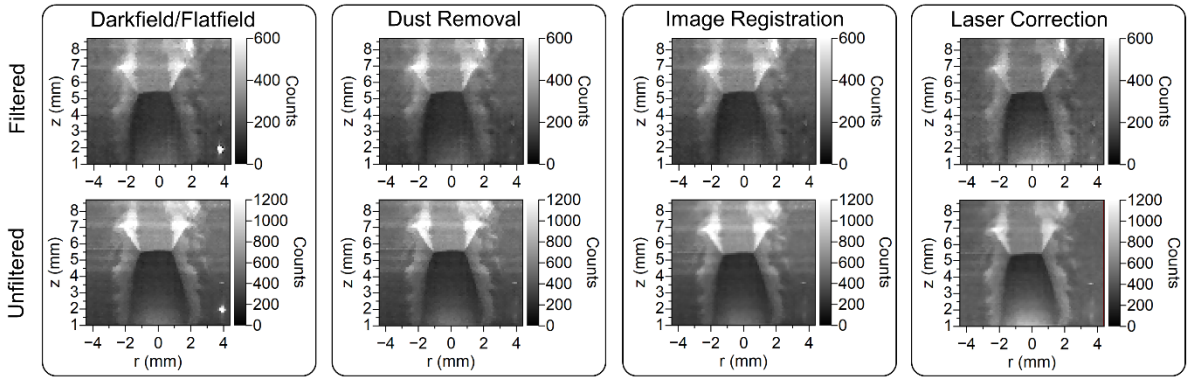

Fig. 5 Simultaneously captured filtered and unfiltered images after the darkfield/flatfield correction, dust removal, image registration, and the laser sheet correction.

B. Wavemeter calibration

The wavemeter had an absolute accuracy in the visible range of 200 MHz (or ~0.0067 cm^{-1}) and required calibration. Due to slight variations in iodine vapor pressure between the two iodine cells, which changed the transmission profile, the wavemeter was calibrated based on the camera iodine cell. Replacing the reference iodine cell with the camera iodine cell in the Frequency Monitoring leg shown in Fig. 2, voltage traces from the filtered and unfiltered PDs were acquired. The voltage measurement of each pulse on the filtered PD was divided by the voltage measured for the same pulse on the unfiltered PD to obtain an experimental transmission profile. Each transmission measurement was normalized by an averaged value where the transmission should be close to 100%, near 18789.35 cm^{-1}. Each transmission measurement was then matched with the appropriate wavemeter measurement in time. Figure 6 shows a raw experimental transmission profile (blue) compared to the theoretical profile generated using the Forkey code [14] demonstrating the necessity for this bulk correction factor. The offset was found by minimizing the total absolute value of the residual between the theoretical value and the experimental value, Fig. 6. The shift that created the minimum absolute residual was found to be 0.022 cm^{-1} which was subtracted from every wavemeter measurement.

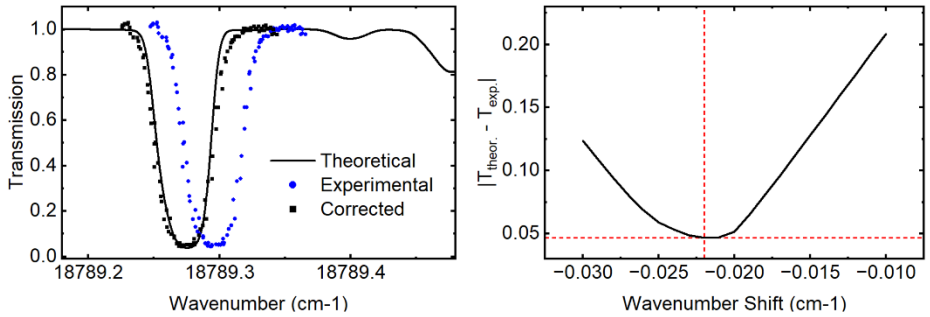

Fig. 6 (Left) Experimental transmission profile before and after wavemeter correction compared to the theoretical prediction. (Right) Determination of the wavemeter deviation correction factor by minimizing the total residual between the theoretical and experimental transmission values.

C. Pressure, temperature, and velocity fitting procedure

Equation (3) describes the FRS intensity, I_{FRS}, using the ideal gas law for density:

$$I_{FRS} = A\left(\frac{M_m}{k_B A_V}\right)\frac{P}{T}\int_{-\infty}^{\infty} S(\nu-\nu_0-\Delta\nu_D(V),P,T,\theta)F(\nu-\nu_0)d\nu + B\int_{-\infty}^{\infty} L(\nu-\nu_0)F(\nu-\nu_0)d\nu \quad (3)$$

where A and B are background parameters, M_m is the molar mass, k_B is the Boltzmann constant, A_V is Avogadro's number, P is the pressure, T is the temperature, $S(\nu-\nu_0-\Delta\nu_D(V),P,T,\theta)$ is the Rayleigh scattering spectral profile at incident laser frequency ν_0, $\Delta\nu_D(V)$ is the Doppler shift due to velocity V, θ is the angle between the camera and laser sheet, and $F(\nu-\nu_0)$ is the filter transmission spectral profile. The Rayleigh scattering spectrum $S(\nu-\nu_0-\Delta\nu_D,\ p,\ T,\ \theta)$ was calculated using the well-known Pan S7 code [15], which has been converted to MATLAB by J. Smith [16]. The iodine transmission profile, $F(\nu-\nu_0)$, was modeled using the Forkey code [14]. The laser profile, $L(\nu-\nu_0)$, was modeled as a Gaussian profile:

$$L(\nu-\nu_0) = \frac{1}{\sigma_L\sqrt{2\pi}}\exp\left[-\frac{(\nu-\nu_0)^2}{2\sigma_L^2}\right] \quad (4)$$

where σ_L is is the standard deviation of the distribution and related to the full-width-at-half maximum (FWHM) by FWHM = $\sqrt{2\ln 8}\,\sigma_L$. The commercial BML used in this work has a specified linewidth of 100–150 MHz therefore an intermediate value of σ_L = 65 MHz was chosen. The Doppler shift, $\Delta\nu_D$, can be related to the velocity using:

$$\Delta\nu_D = \frac{2}{\lambda_0}V\cos\delta\sin\frac{\theta}{2} \quad (5)$$

where δ is the angle between the velocity vector and the k vector and λ_0 is the laser wavelength. In the configuration used, the radial velocity was at an angle of $\delta = 45°$ and the scattering was collected at $\theta = 90°$ from the laser beam.

The extraction of the flow properties using Eq. (3-5) was accomplished in two steps. First, a non-linear least squares algorithm was used to determine the background parameters, A and B, on a pixel-by-pixel basis using FRS images of a reference condition with known pressure, temperature, and velocity (1 atm, 296 K, and 0 m/s). Next, a least squares algorithm was used to find the unknown $P, T,$ and V within the flow field experiment using these A and B values. An example of the fitting steps is shown for a single pixel from data taken using Configuration 1 in Fig. 7.

For the same pixel shown in Fig. 7, the sensitivity of the least squares fit to pressure, temperature, and velocity changes can be explored. In Fig. 8, the obtained fit is compared to a simulated curve fit with increased and decreased values of one parameter while holding the other parameter values constant. The profile is most sensitive to pressure and temperature, especially in the regions further outside the absorption band near 18789.2 cm^{-1} and 18789.35 cm^{-1}. However, the profile is less sensitive to changes in velocity. Two additional calculations of pressure, temperature, and velocity before the Mach disc and near the barrel shock are shown in Fig. 9 to further illustrate the change in the FRS signal intensity in different regions of the flow.

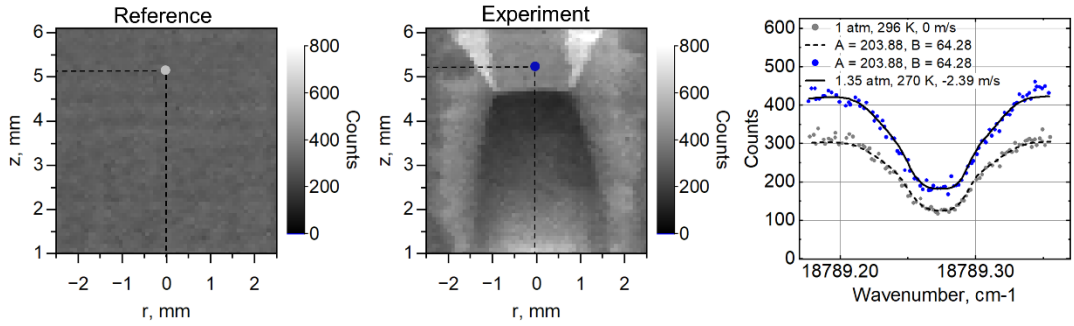

Fig. 7 (Left) Example reference image with a single pixel indicated to determine A and B. (Center) Example flow image used to determine $P, T,$ and V at the same pixel location as the calibration image. (Right) Fitted curves for the reference and flow experiment data overlayed with the intensity data.

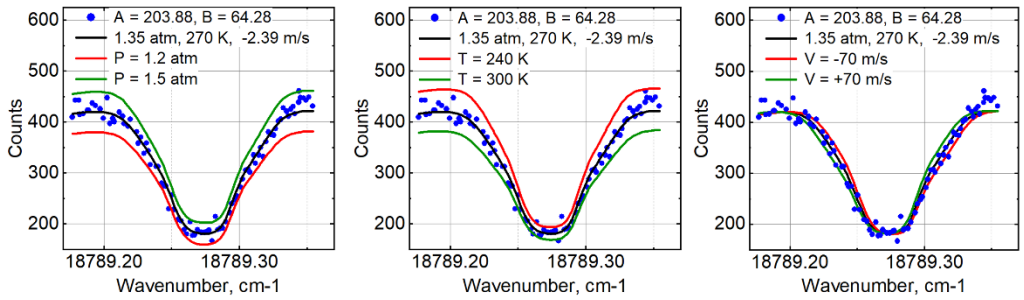

Fig. 8 Comparison between the fitted curve and the curve generated with increased and decreased (left) pressure, (center) temperature, and (right) velocity.

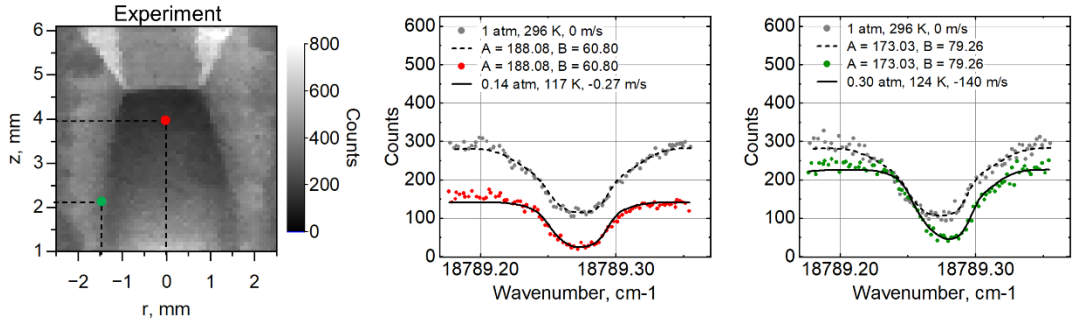

Fig. 9 Additional examples of the FRS signal intensities at different pixel locations. The grey curves are taken from the corresponding pixels in the reference images as shown in Fig. 7 (left).

D. Background subtraction for instantaneous density measurements

Instantaneous density measurements could be acquired from the unfiltered Rayleigh scattering images. Without the filter in place, the intensity of the RS signal is given by Eq. (6):

$$\mathrm{I_{RS}} = A\rho + B \tag{6}$$

$$\rho = \frac{I_{RS}}{I_{RS,ref}}\rho_{ref} \tag{7}$$

The density, ρ, can then be determined using Eq. (7) by comparing the RS signal intensity in the flow to the signal intensity of a reference condition, $I_{RS,ref}$ of known density, ρ_{ref}. However, to use Eq. (7), careful subtraction of the background parameter B must be performed, such as described by [17]. To estimate the background, a moving mean of the top 30 pixels and bottom 100 pixels of each column in the reference and flow images, with linearly interpolated values between the two regions, to form a background "image". This image was subtracted from each unfiltered image. An example of this is shown in Fig. 10 for the static room temperature and pressure air.

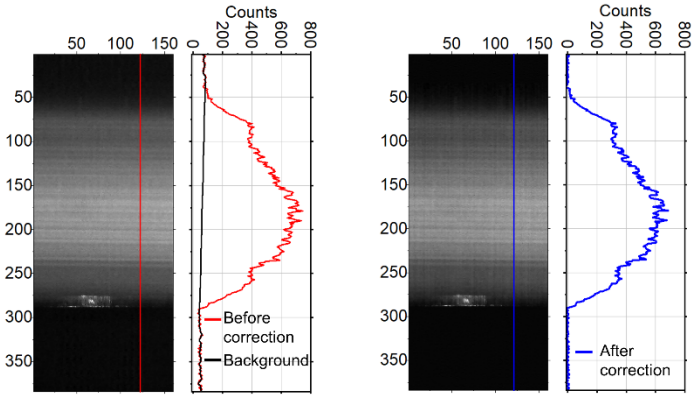

Fig. 10 (Left) Single intensity profile of room temperature and pressure air Rayleigh signal and linear fit for the background intensity. (Right) The same intensity profile after subtraction of the background.

IV. Computational Fluid Dynamics Methodology

A. Empirical centerline pressure, temperature, and density predictions

Calculated centerline pressure, temperature, and density were obtained using correlations, isentropic relations, and normal shock relations and compared with the experimental results. Following the formula given by [18], the Mach number as a function of nozzle diameter, D, from the nozzle exit was calculated. With some variable changes from the original formula given in the paper (to avoid confusion with the A and B variables), the centerline Mach number at z/D from the nozzle exit, is given by Eq. (8), which is limited to at least $1.0D$ from the nozzle exit:

$$M\left(\frac{z}{D}\right) = C_1\left(\frac{z}{D} - \frac{z_0}{D}\right)^{\gamma-1} - \frac{1}{2}\left(\frac{\gamma+1}{\gamma-1}\right)\left[C_1\left(\frac{z}{D} - \frac{z_0}{D}\right)^{\gamma-1}\right]^{-1} + C_2\left(\frac{z}{D} - \frac{z_0}{D}\right)^{-3(\gamma-1)} \tag{8}$$

where $C_1 = 3.65$, $z_0/D = 0.4$, $C_2 = 0.2$, and $\gamma = 1.4$ for air. The pressure, temperature, and density were then calculated using isentropic relations based on the Mach number. The theoretical Mach disc location, $\mathrm{z_{MD}}$, was calculated using two empirical relations. The first is equation (9) given by Crist *et al.* [19] which was found to agree reasonably well experimentally with underexpanded jets from orifice-style nozzles operating at $5 \leq \mathrm{PR} \leq 7$ [20]. The second is Equation (10) given by Gibbings *et al.* [21] for a circular converging nozzle. The flow conditions after the Mach disc at $\mathrm{z_{MD}}$ were then found using normal shock relations.

$$\frac{z_{MD}}{D} = 0.65\sqrt{\mathrm{NPR}} \tag{9}$$

$$\frac{z_{MD}}{D} = 0.84(\mathrm{NPR} - 1.893)^{0.415} \tag{10}$$

B. Computational fluid dynamics

To solve the flow field inside and outside of the nozzle, the Reynolds Averaged Navier Stokes (RANS) equations were solved with the k-ω Shear Stress Transport (SST) turbulence model on a 2D axisymmetric mesh with around 60,000 hexahedral cells with ANSYS FLUENT and meshed with ANSYS ICEM CFD. A series of total pressures of varying magnitudes was applied at the inlet to mimic the different pressure ratios, while a static pressure of 1 atm was applied to the outlet. Walls were treated as viscous with a first layer thickness (y+) of less than 1 at the nozzle walls, to capture the viscous sublayer, see Fig. 11. A small portion of the chamber, as well as a small air volume for the jet, was modeled to capture the exhaust in the experimental setup. Within the Fluent solver, a convergence criterion of 1e-3 was used, and cases were run until residuals plateaued. Additionally, a mesh sensitivity on a 3D domain was performed and compared to the two-dimensional simulations to verify the two-dimensionality of the domain.

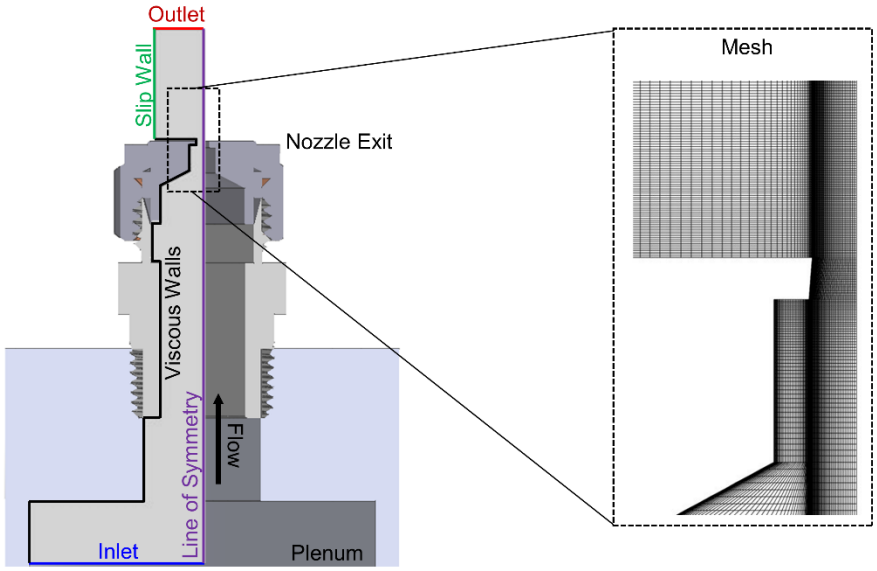

Fig. 11 Boundary conditions for the CFD analysis of the underexpanded jet with the mesh grid depicted in the dashed box.

V. Results and Discussion

A. Configuration 1: Single 5-ms pressure, temperature, radial velocity, and density measurements

The property measurements at NPR of 5, 6, and 7 acquired in 5-ms using Configuration 1 are shown in Fig. 12. Pressure, temperature, and radial velocity were found at each pixel utilizing the methods outlined in Section III. The density measurements were made using two different methods: (i) calculated from the pressure and temperature fields using the ideal gas law, and (ii) averaging the ~90 instantaneous density measurements from the unfiltered RS images. The expected trends in pressure, temperature and radial velocity are all observed: the pressure and temperature decrease with distance from the nozzle exit and then increases across the normal shock wave; the velocity in the core of the jet is near zero along the centerline then increases away from the centerline until the barrel shock is reached. The Mach disc moves further from the exit with increasing NPR. The calculated density and mean density from the unfiltered RS images show excellent qualitative agreement. The CFD results for the pressure, temperature, radial velocity, and density for three NPRs are shown in Fig. 13.

In Fig. 14, the centerline pressure, temperature, and density were compared to both the empirical predictions and the CFD results. The pressure matches well with the CFD and theoretical calculations before the Mach disc, although the CFD appears to capture the slope better for all properties. The correlation given by Crist *et al*. overpredicted the location of the Mach disc; however, this overprediction was also seen in the experimental data by Addy *et al*. specifically for orifice nozzles in [20]. The correlation by Gibbings *et al*. matches both the location and post-Mach disc pressure and density. The measured temperature overall showed more variance than the pressure and, especially for an NPR of 5 and 6, was lower than both the CFD and empirical correlations by ~20 K.

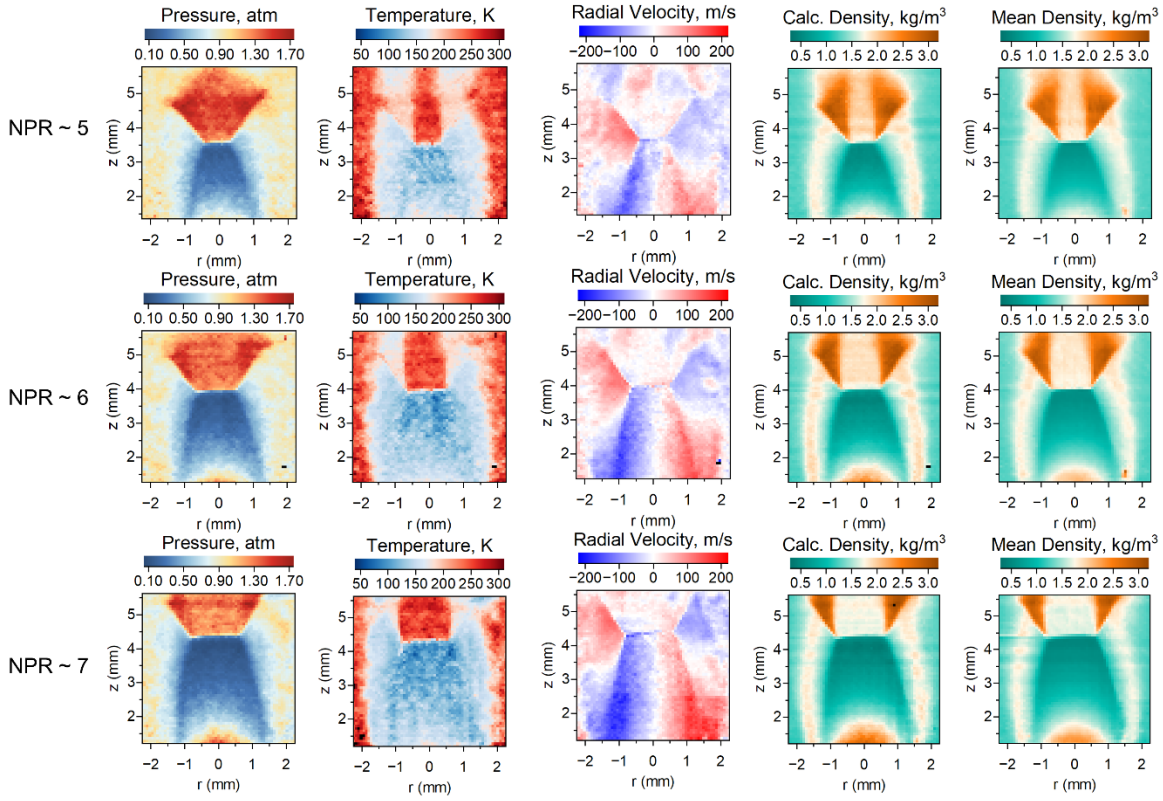

Fig. 13 Pressure, temperature, and radial velocity fields for NPR of 5, 6, and 7 measured across 5-ms using Configuration 1. Calculated density is shown on the same color scale as the mean density.

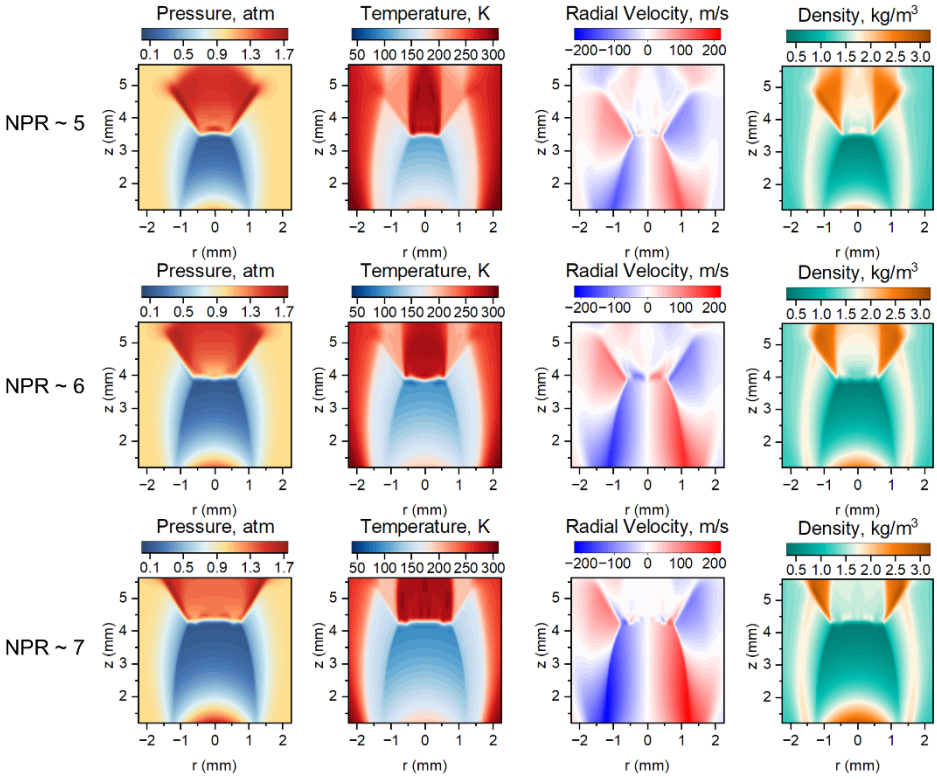

Fig. 12 Computational thermodynamic property fields for NPR of 5, 6, and 7.

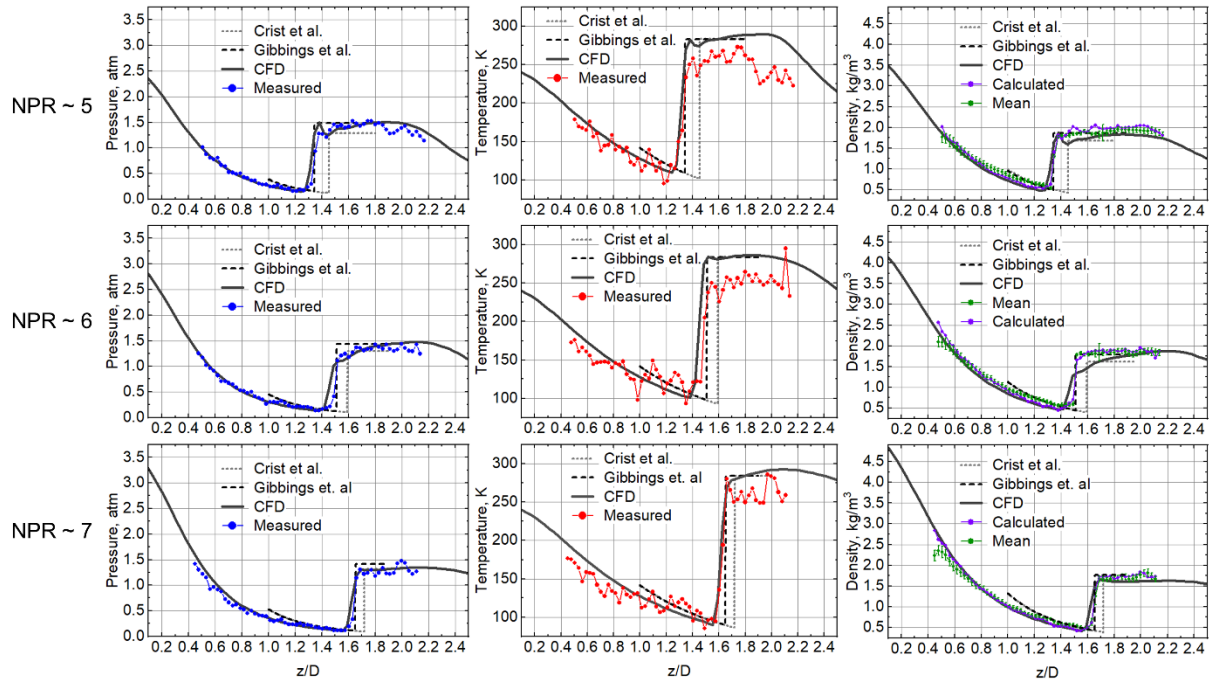

Fig. 14 Centerline pressure, temperature, and mass density for increasing NPR compared to both empirical correlations and CFD results. Error bars indicate one standard deviation across 100 unfiltered images in the 5-ms burst.

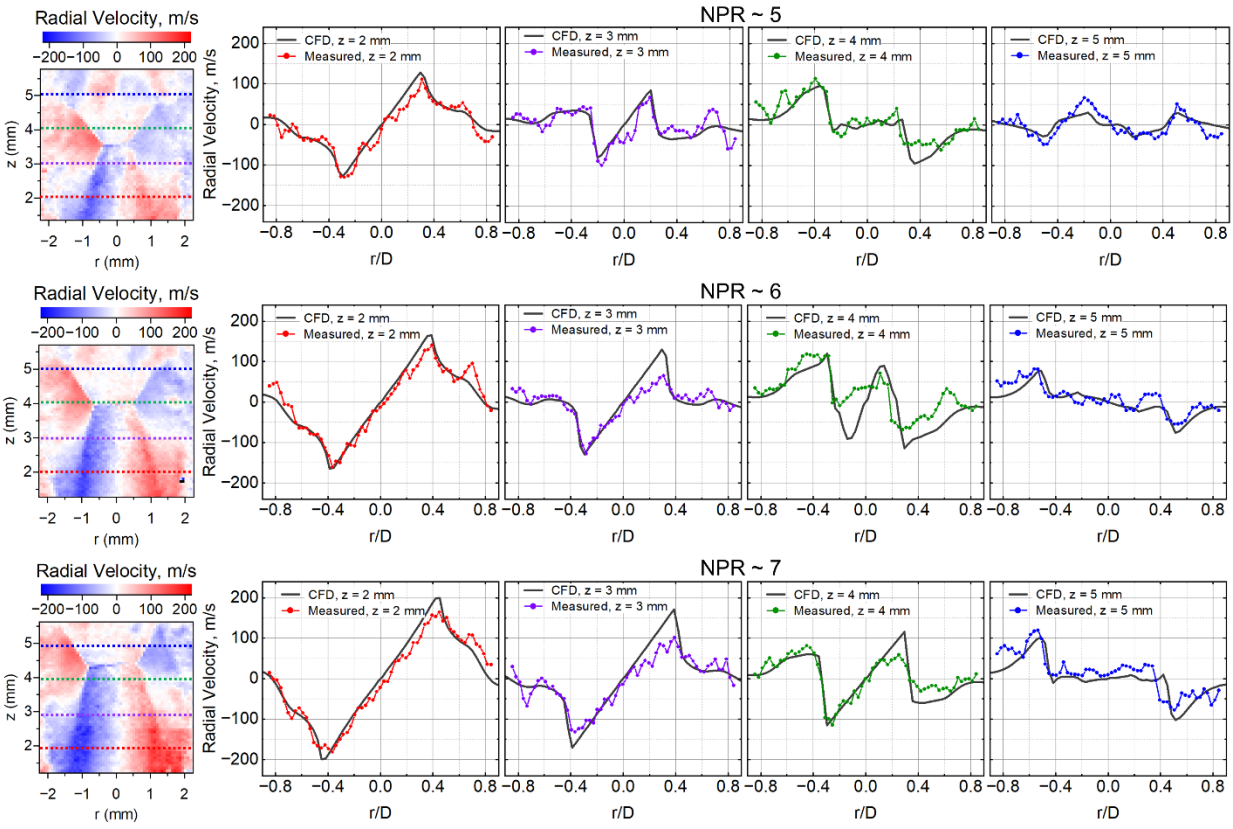

Fig. 15 Configuration 1 measured radial velocity compared to CFD results at four different axial locations.

The density calculated by the ideal gas law agrees within 6% with the mean density from $0.8 \leq z/D$ while the difference increased to ~10-20% closer to the nozzle exit. Most likely, this is also due to the increased background scattering and decreased laser energy in the wings of the laser sheet near the nozzle exit plane which is difficult to accurately subtract from the unfiltered camera images.

The radial velocity was compared to the CFD results at four different axial locations at $z = 2, 3, 4,$ and 5 mm in Fig. 15. Close to the nozzle exit at $z = 2$ mm, the highest radial velocity is seen on either side of the centerline at $r/D = 0$. For the axial location of 4 mm, the NPR of ~6 condition shows the greatest deviation between the CFD and experimental results. After the Mach disc, at $z = 5$ mm, the radial velocity switches direction on either side of the centerline.

B. Configuration 2: Single 1-ms pressure, temperature, radial velocity, and density measurements

The property measurements at PR of 7 acquired in 1-ms using Configuration 2 are shown in Fig. 16, centerline measurements are shown in Fig. 17, and velocity axial profiles are shown in Fig. 18. In this case, the per pulse energy was decreased by ~60% when the laser repetition rate was increased by 10x to 200 kHz from 20 kHz, while the scan time was decreased 5x from 5 ms to 1 ms. The RS intensity is proportional to incident laser energy, so the decreased per-pulse energy decreased the overall signal also by ~60%.

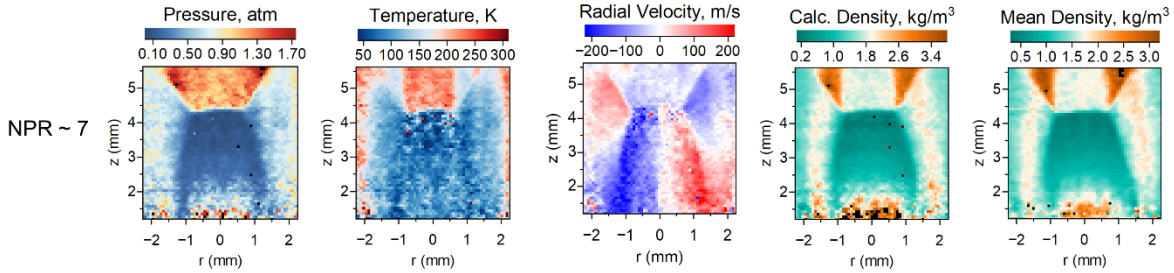

Fig. 16 Pressure, temperature, and radial velocity fields for three different pressure ratios measured across 1-ms using Configuration 2. Calculated density from the pressure and temperature using the ideal gas law is also shown on the same color scale as the mean density found from the unfiltered RS images.

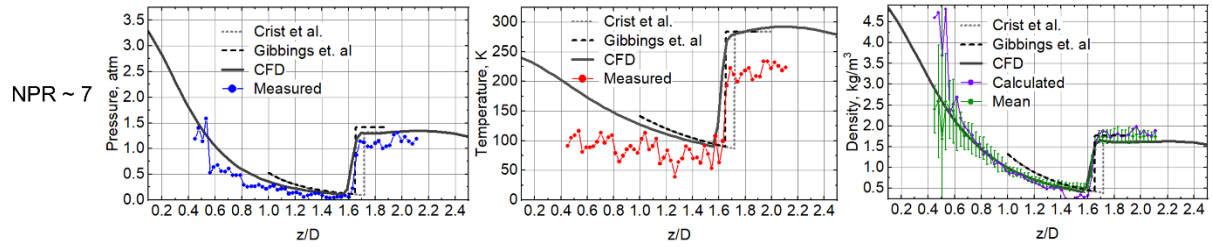

Fig. 17 Centerline pressure, temperature, and density across 1-ms using Configuration 2 for NPR of ~ 7 compared to both empirical calculations and CFD results. Error bars indicate one standard deviation across 200 unfiltered images in the 1-ms burst.

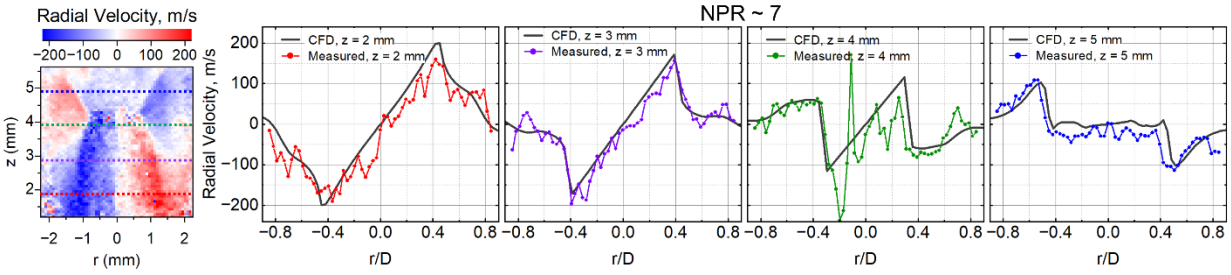

Fig. 18 Measured radial velocity using Configuration 2 compared to CFD results at four different axial locations.

In the low intensity region of the laser sheet near the nozzle exit and in the low-density region before the Mach disc, many of the pixel intensity values were close to the noise level. Consequently, the fit of several pixels failed to converge and are indicated by black pixels. Additionally, the measured temperature was approximately 20% lower than the temperature found with Configuration 1. Due to this, the calculated density was correspondingly higher than the mean density found from the unfiltered RS images. Additionally, the instantaneous density measurements had a much higher amount of shot-to-shot variance near the nozzle exit as indicated by the error bars in Fig. 17. The velocity measurements also showed additional variance with the expected trends. Aside from at $z = 4$ mm, the velocity measurements followed the same trends as the CFD results.

VI. Conclusion

In this work, the feasibility and performance of a frequency-scanning burst-mode FRS system was characterized and explored. By modulating the current of the diode laser seed of a burst-mode laser, the incident laser frequency can be scanned across an iodine absorption line while collecting filtered and unfiltered Rayleigh scattering signal at each frequency step. With known background parameters, the pressure, temperature, and velocity could then be fitted simultaneously. The results were compared to both isentropic and correlation-based calculations as well as a computational fluid dynamic model. The overall flow features that were observed in the experimental thermodynamic property fields agreed with the CFD results.

The millisecond measurement timescales presented, which are ~100,000x faster than what has been previously demonstrated, make frequency-scanning FRS practical for short test duration wind tunnel applications. This method can be extended to multiple scans per burst for more time-resolved measurements of temperature, pressure, and velocity fields by increasing the scan rate which can be accomplished without loss of frequency-resolution by also increasing the laser repetition rate. Initial efforts shown in this work for the faster configuration indicate that increased signal-to-noise will be necessary to achieve this increased temporal resolution.

Acknowledgments

A.M. Braun was supported by a NASA Space Technology Graduate Research Opportunity (NSTGRO) provided by the NASA Space Technology Mission Directorate (STMD). N. S. Rodrigues and P. M. Danehy acknowledge the support of the STMD and the Exploration Systems Development Mission Directorate (ESDMD) *Plume Surface Interaction* project and the NASA Aeronautics Research Mission Directorate (ARMD) Transformative Tools and Technologies (TTT) project. The Burst-Mode laser used for this work was originally procured through a NASA SBIR Phase IIX/III project (NNX15CL24C) and recently upgraded by a NASA Phase IIE/III SBIR (80NSSC20C0099) The authors would like to thank Dr. Ross Burns from the NASA Langley Advanced Measurements and Data Systems Branch, affiliated with the National Institute of Aerospace at the time of the experiment, for helpful discussion on the FRS experimental set-up, W. Holt Ripley from the NASA Langley Advanced Measurements and Data Systems Branch for assistance with build-up of the underexpanded jet facility, and Christopher Crabtree from Spectral Energies, LLC for setting up the burst-mode laser at the NASA Langley Research Center.

References

[1] R. B. Miles, W. R. Lempert, and J. N. Forkey, "Laser Rayleigh scattering," *Meas. Sci. Technol.*, vol. 12, no. 5, pp. R33–R51, May 2001, doi: 10.1088/0957-0233/12/5/201.

[2] M. Boguszko and G. S. Elliott, "On the use of filtered Rayleigh scattering for measurements in compressible flows and thermal fields," *Exp. Fluids*, vol. 38, no. 1, pp. 33–49, Jan. 2005, doi: 10.1007/s00348-004-0881-4.

[3] U. Doll, R. Kapulla, J. Steinbock, M. Dues, M. Migliorini, and P. K. Zachos, "Seeding-free inlet flow distortion measurement by filtered Rayleigh scattering: diagnostic approach and verification," in *AIAA SCITECH 2023 Forum*, National Harbor, MD & Online: American Institute of Aeronautics and Astronautics, Jan. 2023. doi: 10.2514/6.2023-1372.

[4] G. S. Elliott and M. Samimy, "Rayleigh scattering technique for simultaneous measurements of velocity and thermodynamic properties," *AIAA J.*, vol. 34, no. 11, pp. 2346–2352, Nov. 1996, doi: 10.2514/3.13400.

[5] J. George, T. P. Jenkins, and J. A. Sutton, "Simultaneous Multi-Property Laser Diagnostics using Filtered Rayleigh Scattering," in *32nd AIAA Aerodynamic Measurement Technology and Ground Testing Conference*, Washington, D.C.: American Institute of Aeronautics and Astronautics, Jun. 2016. doi: 10.2514/6.2016-3110.

[6] J. N. Forkey, N. D. Finkelstein, W. R. Lempert, and R. B. Miles, "Demonstration and characterization of filtered Rayleigh scattering for planar velocity measurements," *AIAA J.*, vol. 34, no. 3, pp. 442–448, Mar. 1996, doi: 10.2514/3.13087.

[7] U. Doll, G. Stockhausen, and C. Willert, "Endoscopic filtered Rayleigh scattering for the analysis of ducted gas flows," *Exp. Fluids*, vol. 55, no. 3, p. 1690, Mar. 2014, doi: 10.1007/s00348-014-1690-z.

[8] U. Doll, G. Stockhausen, and C. Willert, "Pressure, temperature, and three-component velocity fields by filtered Rayleigh scattering velocimetry," *Opt. Lett.*, vol. 42, no. 19, p. 3773, Oct. 2017, doi: 10.1364/OL.42.003773.

[9] T. W. Fahringer, R. A. Burns, P. M. Danehy, P. M. Bardet, and J. Felver, "Pulse-Burst Cross-Correlation Doppler Global Velocimetry," *AIAA J.*, vol. 58, no. 6, pp. 2364–2369, Jun. 2020, doi: 10.2514/1.J059172.

[10] N. S. Rodrigues, P. M. Danehy, N. Jiang, P. Hsu, J. Leicht, and S. Roy, "100 kHz High-Spectral-Resolution NO-PLIF Measurements for Compressible Flows," in *AIAA SCITECH 2023 Forum*, National Harbor, MD & Online: American Institute of Aeronautics and Astronautics, Jan. 2023. doi: 10.2514/6.2023-0405.

[11] R. A. Burns, T. W. Fahringer, and P. M. Danehy, "Velocity measurements across an oblique shock using pulse-burst cross-correlation DGV," in *AIAA Scitech 2021 Forum*, American Institute of Aeronautics and Astronautics. doi: 10.2514/6.2021-0120.

[12] C. Dedic, A. D. Cutler, and P. M. Danehy, "Characterization of supersonic flows using hybrid fs/ps CARS," in *AIAA Scitech 2019 Forum*, American Institute of Aeronautics and Astronautics. doi: 10.2514/6.2019-1085.

[13] C. J. Peters, R. A. Burns, R. B. Miles, and P. M. Danehy, "Effect of low temperatures and pressures on signal, lifetime, accuracy and precision of femtosecond laser tagging velocimetry," *Meas. Sci. Technol.*, vol. 32, no. 3, p. 035202, Dec. 2020, doi: 10.1088/1361-6501/abc577.

[14] J. N. Forkey, W. R. Lempert, and R. B. Miles, "Corrected and calibrated I_2 absorption model at frequency-doubled Nd:YAG laser wavelengths," *Appl. Opt.*, vol. 36, no. 27, pp. 6729–6738, Sep. 1997, doi: 10.1364/AO.36.006729.

[15] X. Pan, "Coherent Rayleigh -Brillouin scattering," Ph.D., Princeton University, United States -- New Jersey. Accessed: Oct. 02, 2022. [Online]. Available: https://www.proquest.com/docview/288218480/abstract/979264AD467A43BFPQ/1

[16] J. Smith, "Coherent+Spontaneous Rayleigh-Brillouin Scattering Spectra (https://www.mathworks.com/matlabcentral/fileexchange/29108-coherent-spontaneous-rayleigh-brillouin-scattering-spectra), MATLAB Central File Exchange." 2010.

[17] T. A. McManus, "An Experimental Investigation of the Relationship between Flow Turbulence and Temperature Fields in Turbulent Non-Premixed Jet Flames," Ph.D., The Ohio State University, United States -- Ohio, 2019. Accessed: Aug. 17, 2023. [Online]. Available: https://www.proquest.com/docview/2320936875/abstract/840C785815A74841PQ/1

[18] H. Ashkenas and F. S. Sherman, "Structure and utilization of supersonic free jets in low density wind tunnels," vol. No. NASA-CR-60423, 1965.

[19] S. Crist, D. R. Glass, and P. M. Sherman, "Study of the highly underexpanded sonic jet.," *AIAA J.*, vol. 4, no. 1, pp. 68–71, 1966, doi: 10.2514/3.3386.

[20] A. L. Addy, "Effects of axisymmetric sonic nozzle geometry on Mach disk characteristics," *AIAA J.*, vol. 19, no. 1, pp. 121–122, 1981, doi: 10.2514/3.7751.

[21] C. Gibbings, J, Ingham, and D. Johnson, "Flow in a Supersonic Jet expanding from a Convergent Nozzle," 2002. Accessed: Nov. 15, 2023. [Online]. Available: https://www.semanticscholar.org/paper/Flow-in-a-Supersonic-Jet-expanding-from-a-Nozzle-Gibbings-J./209d30dadd5396a1931814318047b62e827f7277